RSC Advances

PAPER

View Article Online
View Journal | View Issue

Cite this: *RSC Adv.*, 2024, **14**, 15337

MOF-modified dendrite-free gel polymer electrolyte for zinc-ion batteries†

Changmiao Huang, Hui Li, Zixuan Teng, Yushu Luo and Wanyu Chen *

Zinc-ion batteries are promising candidates for large-scale energy storage, and gel polymer electrolytes (GPEs) play an important role in zinc-ion battery applications. Metal–organic frameworks (MOFs) are characterized by large specific surface areas and ordered pores. This highly ordered microporous structure provides a continuous transport channel for ions, thus realizing the high-speed transmission of ions. In this paper, an MOF-modified dendrite-free GPE was designed. The incorporation of MOF particles not only reduces the crystallinity of the polymer, increases the motility of the molecular chains, and facilitates the transfer of Zn^{2+}, but also attracts anions to reduce polarization during electrochemical reactions. It was shown that this MOF-modified gel polymer electrolyte has a higher ionic conductivity compared to other PVDF-based polymer electrolytes (approximate range of 2×10^{-4} to 3×10^{-3} S cm^{-1}), with a very high conductivity (1.63 mS cm^{-1}) even at −20 °C. The Zn/Zn symmetric cell could maintain operation for more than 3600 h at a current density of 1 mA cm^{-2}, and SEM showed that the MOF-modified gel electrolyte had uniform Zn^{2+} deposition.

Received 22nd March 2024
Accepted 29th April 2024

DOI: 10.1039/d4ra02200a

rsc.li/rsc-advances

Introduction

The excessive consumption of fossil fuels aggravates the energy crisis, and renewable energy sources such as solar, wind power, and tidal energy require the support of energy storage devices since they highly rely on time and location.[1–4] Therefore, electrochemical energy storage devices, such as batteries and supercapacitors, play a crucial role in overcoming the worldwide energy challenges and realizing sustainable development.[5–8] Currently, zinc-ion batteries (ZIBs) have become a hot research topic in battery systems due to their advantages of low cost, high safety, and environment-friendliness.[9–12] Additional enthusiasm for ZIBs has been motivated by the unique advantages of metallic Zn, such as high theoretical capacity (820 mA h g^{-1} and 5855 mA h cm^{-3}), higher redox potential ($E_0 = -0.76$ V *vs.* standard hydrogen electrode), high abundance (about 300 times higher than lithium), and insensitivity to oxygen and a humid atmosphere, which broadens the range of applicable electrolytes.[13–17]

As one of the most important components of a battery, electrolytes provide the basic operating environment to guarantee the transmission of Zn^{2+} between the cathode and Zn anode during the charge–discharge processes. Electrolytes can be categorized into liquid electrolytes and gel electrolytes. Liquid electrolytes are widely used in ZIBs due to their high ionic conductivity, which reaches up to 7–60 mS cm^{-1}.[18–20] However, most aqueous electrolytes still have a large amount of free water in them,[21,22] which will continually erode the Zn anode to produce H_2, resulting in poor compatibility.[23–25] In addition, liquid electrolyte electrical properties are poor at low temperatures because most conventional liquid electrolytes based on aqueous solutions or organic solvents will freeze, resulting in insufficient ionic conductivity below the freezing point.[26–28] Compared with conventional liquid electrolytes, gel polymer electrolytes (GPEs) are mainly composed of a polymer matrix solvent containing electrolyte salts and additives.[29,30] Although the gel polymer electrolyte has a liquid component, it also has a certain geometrical shape, strength, elasticity, *etc.*, and the ionic conductivity is greatly improved compared with the pure polymer electrolyte.[31,32] The entangled polymer chains in the gel polymer impart viscoelasticity to the electrolyte, thereby inhibiting the electroconvection of the fluid and modulating the ionic flux. In addition, due to its three-dimensional network structure, the gel polymer electrolyte can inhibit the growth of zinc dendrites in zinc-ion batteries.[33,34]

Most current aqueous zinc-ion batteries still have various challenges at low temperatures, especially the sharp drop in ionic conductivity at low temperatures. Therefore, addressing the low conductivity of electrolytes at low temperatures is an important aspect. Ionic liquids (ILs) are potential alternatives to aqueous electrolytes due to their good thermodynamic stability, high ionic conductivity, non-flammability and non-volatility.[35] ILs are

School of Materials Science and Engineering, Wuhan University of Technology, Wuhan 430070, China. E-mail: chenwanyu@whut.edu.cn

† Electronic supplementary information (ESI) available. See DOI: https://doi.org/10.1039/d4ra02200a

organic salts composed of organic cations and organic/inorganic anions, also known as low-temperature molten salts.[36,37] With these advantages, ILs are currently used as electrolyte components in metal-ion batteries.[38–40] However, the main disadvantage of using ILs as an electrolyte material is their relatively high viscosity, which can inhibit charge transport in the electrolyte.[41] Therefore, high ionic conductivity and chemical stability of electrolytes based on ILs deserve further investigation.

Metal–organic frameworks (MOFs) are also a way to improve the low-temperature conductivity of electrolytes.[42,43] MOFs are a class of crystalline porous materials with a periodic network structure formed by interconnecting inorganic metal centers (metal ions or metal clusters) with bridging organic ligands through self-assembly.[44–46] The tunable porous structure and high specific surface area of MOFs provide an ideal structure for ionic conductivity, so MOFs can enhance the ionic conductivity performance of electrolytes and promote the migration and transport of ions in electrolytes.[47–49] Therefore, they can be used as inorganic fillers in combination with polymer matrices to improve the low-temperature conductivity of gel polymer electrolytes. Meanwhile, inorganic particles not only inhibit polymer crystallinity and form ion transport pathways at the interface or within the polymer electrolytes; they also compensate for the degradation of mechanical properties caused by low polymer crystallinity.[50] In addition, the use of MOFs as an additive can reduce the polarization effect of the battery, which helps to improve its cycling stability and safety.[51] MOFs have been used in Li-ion batteries due to their tunable porous structure and high specific surface area. However, the use of MOFs as electrolyte materials in Zn-ion batteries has been rarely investigated, and they have mostly been used in the diaphragm modification of ZIBs or in zinc anode modification. For example, Liu *et al.*[52] successfully developed a MOF series of functionalized electrostatically spun polyacrylonitrile nanofiber diaphragms through a precision surface grafting strategy and used them as diaphragms for high-efficiency aqueous zinc-ion batteries.

Herein, a MOF-modified dendrite-free GPE was designed, in which ZIF-8 MOF absorbed an ionic liquid organic electrolyte and then was introduced into a PVDF-HFP matrix to prepare the GPE (named PHILZM). Compared to GPE without MOF nanoparticles (named PHILZ), PHILZM exhibited high ionic conductivity even at low temperatures. The use of PHILZM in the Zn/Zn symmetric cell resulted in better cycling stability and longer cycling time than PHILZ, which indicated that ZIF-8 was effective in inhibiting zinc dendrites as well as side reactions. The enhancement of the electrical properties as well as the cycling performance of the gel electrolyte by the addition of ZIF-8 particles was investigated by N_2 adsorption–desorption, DSC, XRD, SEM and AFM tests. The results showed that the incorporation of MOF provided an ordered mesoporous structure that facilitated the rapid diffusion of ions within it, thus improving the ionic conductivity of the electrolyte. It also inhibited the side reactions at the electrode interface and reduced electrode polarization. As a result, the cycle time of PHILZM symmetric batteries was three times higher than that of gel electrolytes without MOFs.

Results and discussion

Synthesis of gel polymer electrolyte

The gel polymer electrolyte was synthesized by a simple solution-casting method and was translucent, as shown in Fig. 1. The gel polymer electrolyte with MOF nanoparticles were named PHILZM, and the gel polymer electrolyte without MOF nanoparticles was named PHILZ.

The morphology and XRD patterns of ZIF-8 are shown in Fig. 2(a and b). ZIF-8 has an average particle size of 74 nm (Fig. S2, ESI†). As shown in Fig. 2(a), the spatial shape of ZIF-8 was rhombic dodecahedron, with a positive charge (about 24.1 mV, Fig. S1 and Table S2, ESI†). The larger the particle size, the more regular the shape of ZIF-8 became. The X-ray diffractogram (Fig. 2(b)) showed that the ZIF-8 XRD peaks synthesised in this paper matched both the standard card in the crystal library and the ZIF-8 XRDs reported in other literature,[53–56] with distinctive 110, 200, 211, 220, 310, and 222 facets, indicating the successful synthesis of the purer ZIF-8. The prepared ZIF-8 had (110) facets, corresponding to the 12 exposed facets in the SEM.

The gel polymer electrolyte was tested by infrared spectroscopy. As shown in Fig. 2(c), the characteristic peaks of the PVDF-HFP matrix all appeared in the spectrum of the PHIILZM matrix, indicating that the addition of ZIF-8 particles did not affect the functional group structure of the pristine polymer. The peaks at 1410, 1170, and 1070 cm^{-1} could be attributed to the bending vibration of $-CH_2$, the asymmetric stretching of $-CF_2$, and the crystalline phase, respectively. The peak at 1660 cm^{-1} could be attributed to the C=C stretching vibration of the imidazole ring, and the peak near 3150 cm^{-1} could be attributed to C–H stretching. The broad peak near 3450 cm^{-1} was related to the telescopic vibration of N–H. The peaks at 1570 cm^{-1} and 1170 cm^{-1} were associated with the stretching vibration of the C=N group and the C–N group, respectively, and corresponded to the characteristic peaks of ionic liquids. The in-plane bending vibration peaks at 1300 and 1170 cm^{-1} and the out-of-plane bending vibration at 750 and 690 cm^{-1} for the imidazole ring could be observed distinctly. The out-of-plane imidazole ring bending peaks below 800 cm^{-1} come from the nanoparticles, where the 426 cm^{-1} N–H stretching corresponds to the most dominant structure of the ZIF-8 framework. However, in the nanocomposite gel polymer electrolyte PHZILM, the N–H stretching was slightly blue-shifted, and the absorption peaks were weakened. The above results were mainly attributed to the electrostatic interaction between the BF_4^- anions and Zn metal clusters in the ionic liquid weakening the interaction between the Zn metal centers and the linker molecules.[57]

Conductivity properties of gel polymer electrolytes

EIS diagrams were used to calculate the ionic conductivity. Fig. 3(a), S3 and S4 (ESI)† show the ionic conductivity of the PHILZM and PHILZ at different temperatures. Fig. S3† shows that the component with PVDF-HFP/ILs/MOF = 1 : 3 : 1 had a higher ionic conductivity compared to the other components.

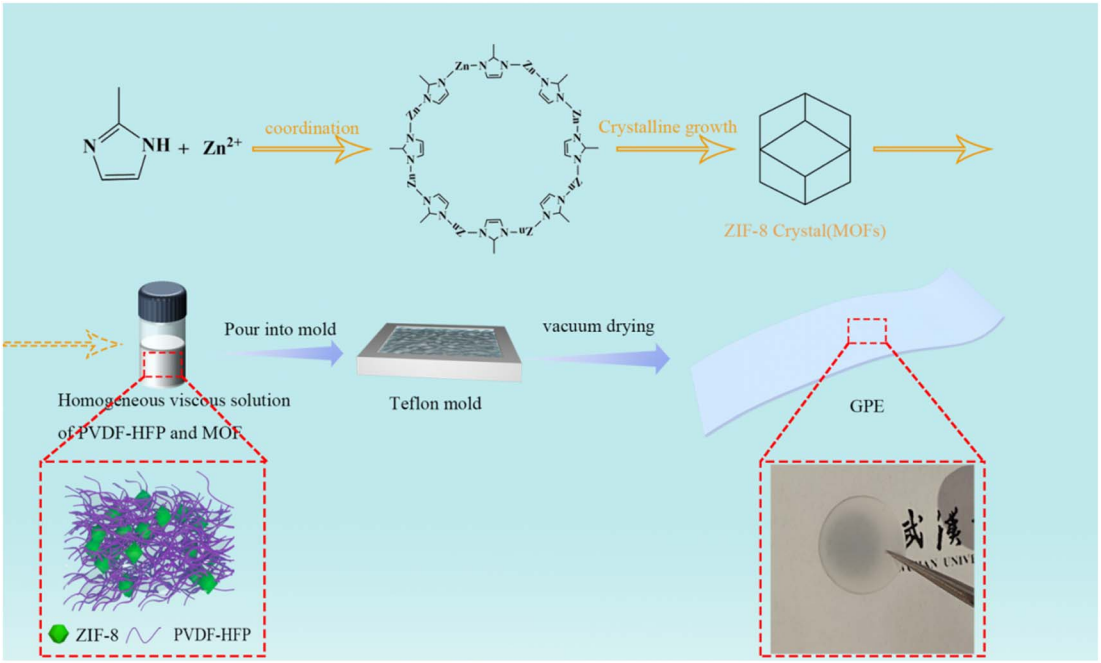

Fig. 1 Synthesis of gel polymer electrolyte.

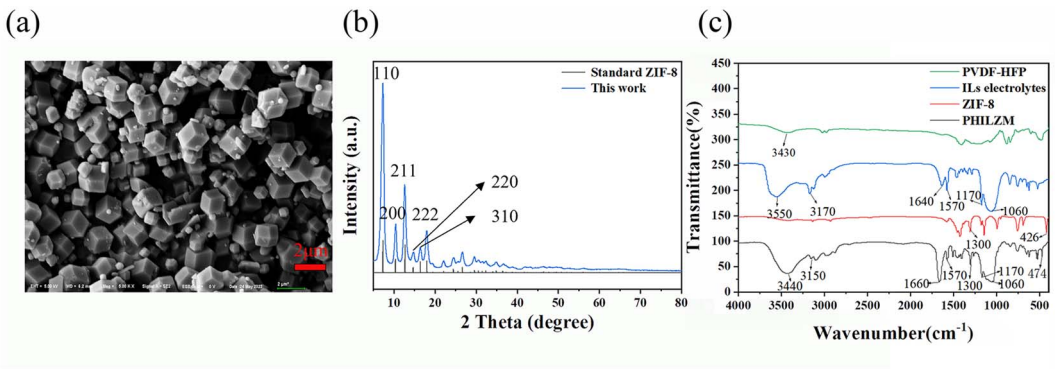

Fig. 2 (a) SEM image of ZIF-8. (b) XRD of ZIF-8. (c) FTIR spectrum of the gel polymer electrolytes.

From Fig. 3(a), it could be seen that the ionic conductivity of the gel electrolyte increased with increasing temperature, and the ionic conductivities of PHILZM were higher than those of PHILZ at each temperature. For example, PHILZM exhibited 1.9 times higher ionic conductivity than PHILZ (1.63×10^{-3} S cm^{-1} *vs.* 8.58×10^{-4} S cm^{-1}) at low temperature (−20 °C). The ionic conductivities of PHILZM and PHILZ at 0 °C were 3.68×10^{-3} S cm^{-1} and 3×10^{-3} S cm^{-1}, respectively. However, both PHILZM and PHILZ exhibited low conductivity (<2×10^{-4} S cm^{-1}) when the temperature dropped below −40 °C. This would be related to the crystallization of the molecular chains.[58] The ionic conductivity of PHILZM was 7.3×10^{-3} S cm^{-1} at room temperature, which is higher compared with other PVDF-HFP-based polymer electrolytes (Table S1, ESI†). Two reasons could make the ionic conductivity of PHILZM higher than that of PHILZ. One factor is mainly attributed to the porous structure of MOF nanoparticles, which facilitated ion transport, enabling PHILZM to have better conductivity than PHILZ.[59,60] As shown in Fig. 3(b), the N_2 adsorption–desorption profile of ZIF-8 exhibited typical microporous structural features without hysteresis loops, corresponding to a specific surface area of 1020.1 m^2 g^{-1} and a pore volume of 0.36 cm^{-3} g. ZIF-8 nanoparticles had extremely high specific surface area and porosity, which meant that more ion transport paths were available per unit mass of particles. As a result, an electrolyte containing the MOF had more ion transport paths under the same conditions, which increased the overall ionic conductivity.[61] The metal ions and organic ligands in ZIF-8 build a reticular three-dimensional skeleton. As can be seen in Fig. 3(c), the average pore size of the ZIF-8 particles was 1.77 nm, and this pore structure provided a continuous channel in which zinc ions (0.082 nm) were able to move freely, thus increasing their conductivity.[62,63] In addition, according to the Lewis acid-base theory, Zn^{2+} could be regarded as a Lewis acid in nano ZIF-8, which could form a ligand bond with the anion, thus restricting the movement of the anion and releasing more free Zn^{2+} to participate in ion transport.[64]

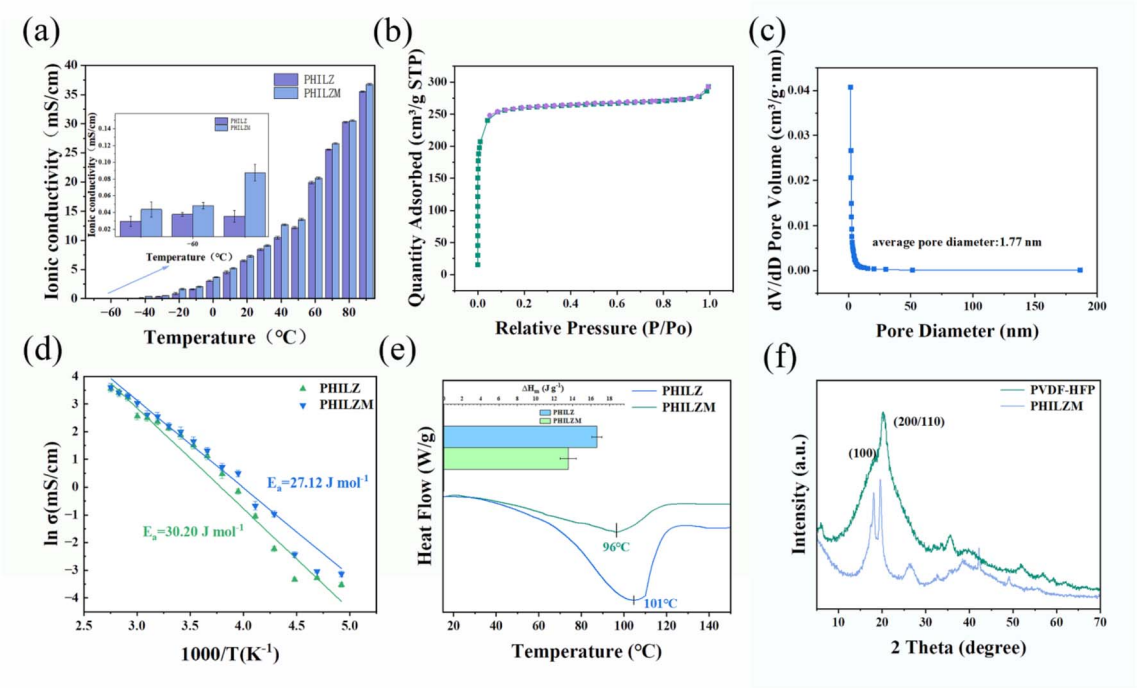

Fig. 3 (a) The ionic conductivities of PHILZM and PHILZ. (b) BET curves of ZIF-8. (c) Pore size distribution of ZIF-8. (d) The ionic conductivity–temperature curve of the gel polymer electrolytes fitted by the Arrhenius formula. (e) DSC of PHILZ and PHILZM. (f) XRD of PVDF-HFP and PHILZM.

Secondly, the molecular motion of the polymer chain segments could have an effect on ion transport. Ions had greater mobility as they moved along the polymer chain segments. As the polymer chain expanded at higher temperatures, charge carriers were able to move more easily, and therefore, ionic conductivity increased.[65] The ionic conductivity was fitted using the Arrhenius formula:

$$\sigma = A \exp[-E_a/RT],$$

where σ is the conductivity; A and R are constants—A is the frequency factor, and R is the molar gas constant; E_a is the activation energy required for the conduction process. It could be seen from Fig. 3(d) that the curve was fitted to the Arrhenius formula with decent linearity at high temperatures but with severe deviation at low temperatures due to crystallization of the molecular chains. Further activation energies calculated by the Arrhenius formula showed that the activation energy of PHILZM (27.12 J mol^{-1}) was less than that of PHILZ (30.20 J mol^{-1}), which suggested a faster kinetic behavior of the molecular chains in the PHILZM gel polymer electrolyte.

It could be observed from the DSC diagram (Fig. 3(e)) that the melting temperature and enthalpy of melting of PHILZM (96 °C, 13.52 J g^{-1}) were slightly lower than those of PHILZ (101 °C, 16.64 J g^{-1}). The enthalpy of melting is related to the crystallinity, indicating that PHILZM is less crystalline than PHILZ. The interaction of the Lewis acidic center Zn element in ZIF-8 with the Lewis basic center F element in the PVDF-HFP chain segments reduced the symmetry of PVDF-HFP, leading to reduced crystallinity and increased chain segment motion, which improved the transport of Zn^{2+}.[66] Moreover, the XRD spectra (Fig. 3(f)) of PVDF-HFP and PHILZM showed two specific diffraction peaks at 18.1° and 20.2°, corresponding to the (100) face of the α-phase and the (200/110) face of the β-phase of PVDF-HFP, respectively.[67] The decrease in intensity and half-width of the two peaks in PHILZM suggested that the incorporation of MOF particles reduced the crystallinity of the polymer electrolyte.[68] The low crystallinity indicated that the polymer chains could move faster in PHILZM, meaning that the zinc ions could migrate more efficiently. The DSC results of Fig. 3(e) and the XRD results of Fig. 3(f) were also in agreement with the results calculated from the Arrhenius formula, both demonstrating the fact that the zinc ions in PHILZM had greater mobility when they moved along the polymer chain segments.

Cycling stabilities of Zn/Zn symmetric cells

Zn/Zn symmetric cells were employed to estimate the Zn^{2+} stripping/plating performance of the gel polymer electrolyte. As shown in Fig. 4(a) and S5 (ESI),† the symmetrical cells assembled with PHILZM exhibited great cycling stability and low polarization voltage (~20 mV) for nearly 3600 hours at a current density of 1 mA cm^{-2} and a capacity density of 1 mA h cm^{-2}. In contrast, symmetrical batteries using PHILZ could only cycle for just under 1000 hours. At a current density of 5 mA cm^{-2} (Fig. 4(b) and S6, ESI†), a symmetrical battery with PHILZM could be operated for more than 3000 hours, and the polarization voltage increased less (~10 mV) with cycling. However, the cycle life of symmetrical batteries using PHILZ was only about 800 hours, and the polarization voltage fluctuated widely. This suggested that the

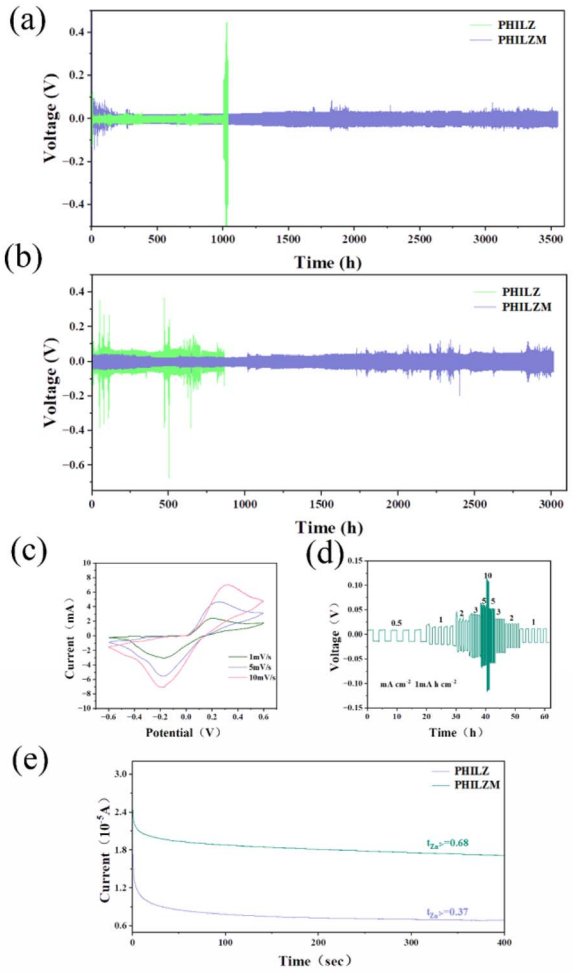

Fig. 4 Galvanostatic Zn plating/stripping in Zn/Zn symmetrical cells with (a) 1 mA cm^{-2}, 1 mA h cm^{-2}, (b) 5 mA cm^{-2}, 5 mA h cm^{-2}. (c) CV curves of the Zn/Ti cell at different scan rates. (d) Rate performance of Zn/Zn cells with PHILZM. (e) CA curves of PHILZM and PHILZ.

addition of MOF gave PHILZM a longer cycle time and more stable cycling stability. ZIF-8 has a highly ordered pore structure in which ions could move freely. This structure helped to increase the transport rate of zinc ions in the electrolyte, thereby reducing the polarization effect during battery cycling. In addition, ZIF-8 could form a more stable interface with the electrode material, which helped to reduce the interfacial resistance between the electrode and the electrolyte.[69]

To understand the reversibility of Zn plating/stripping chemistry, a Zn/Ti asymmetric cell was formed using PHILZM as an electrolyte, and its electrochemical behaviour was measured by cyclic voltammetry (CV). Fig. 4(c) shows the cyclic voltammetry curves of the asymmetric cell at a scanning rate of 1, 5 and 10 mV s^{-1}. As shown, the Zn/Ti asymmetric cell system exhibited obvious redox peaks. With the increase of the number of scanning cycles and the scanning rate, the peak position values of the oxidation peaks and the reduction peaks changed less. It was shown that PHILZM, as an electrolyte, exhibited a reversible redox reaction. Fig. S9 (ESI)† shows the electrochemical window of 2.6 V for PHILZM. To demonstrate that PHILZM has some multiplicative performance, Fig. 4(d) and S8 (ESI)† shows the results of increased current density from 0.5 mA cm^{-2} to 10 mA cm^{-2}. PHILZM had excellent multiplier performance and very stable polarization voltage. When the current density decreased, the polarization curve had good repeatability at the same current density. In contrast, the PHILZ polarization voltage was unstable, and reproducibility was poor compared to PHILZM when reduced to the same current density (Fig. S8, ESI†). The charge transfer assumed by zinc ions could reflect the unique charging and discharging characteristics of conventional batteries. In addition to limiting the increase in energy and power density, a lower zinc ion transfer number caused more anions to accumulate on the electrode surface, increasing concentration polarization and thus the overpotential. This would exacerbate the formation of zinc dendrites.[70] Therefore, the increase in the mobility number of zinc ions was favorable for the conductivity as well as electrochemical stability of the electrolyte. The chronoamperogram (CA) tests at a constant overpotential of 10 mV for 400 s based on PHILZ and PHILZM are shown in Fig. 4(d) and S9 (ESI).† It was observed that PHILZM had a higher zinc ion mobility number ($t_{Zn^{2+}}$: 0.68 *vs.* 0.37) compared to PHILZ. In addition, the curve based on PHILZM was smoother, which meant that PHILZM could effectively reduce the polarization concentration on the anode surface and obtain more uniform ion concentration and deposition morphology.

To further understand the role of PHILZ and PHILZM on the deposition of zinc ions, the symmetric cell metal was characterized after 1000 hours of cycling. The ZIF-8-doped gel polymer electrolyte modulated ion transport to obtain more uniform ion concentration and deposition morphology. The gel polymer electrolytes have good tensile properties (Fig. S10, ESI†) and were advantageous in preventing zinc dendrite growth. The schematics of galvanization on the Zn anode in Zn/Zn symmetric cells with PHILZ and PHILZM are shown in Fig. 5(a). Generally, zinc dendrites are formed due to the initial uneven surface of the substrate, and as charging and discharging proceeds, zinc ions are more likely to migrate to the protruding tips of the electrode surfaces due to the tip effect, which ultimately become the nucleation sites of zinc dendrites.[71] Zn anode optical images showed that PHILZM has a smoother and flatter surface (Fig. 5(b)). Fig. 5(c–j) shows the morphological evolution of the Zn anode with plating time. The surface of the Zn anode in the initial state was polished to remove the oxide layer. As shown in Fig. 5(d), the surface of the Zn anode of the symmetric cell using the PHILZ suffered from inhomogeneous deposition, and larger protrusions could be observed through the high-magnification scanning electron microscope, in Fig. 5(e). In contrast, the surface of the zinc anode was smooth and flat after 1000 hours of cycling in the symmetrical battery with PHILZM (Fig. 5(g)). Through the scanning electron microscope (SEM) with higher magnification (Fig. 5(h)), it could be seen that an organic layer was generated on the surface of the zinc anode, covering the anode surface, which may be related to the generation of SEI.[72] This SEI layer (Fig. S11, ESI†) is characterised by small nodular particles embedded in the polymeric framework.[73,74] The above results

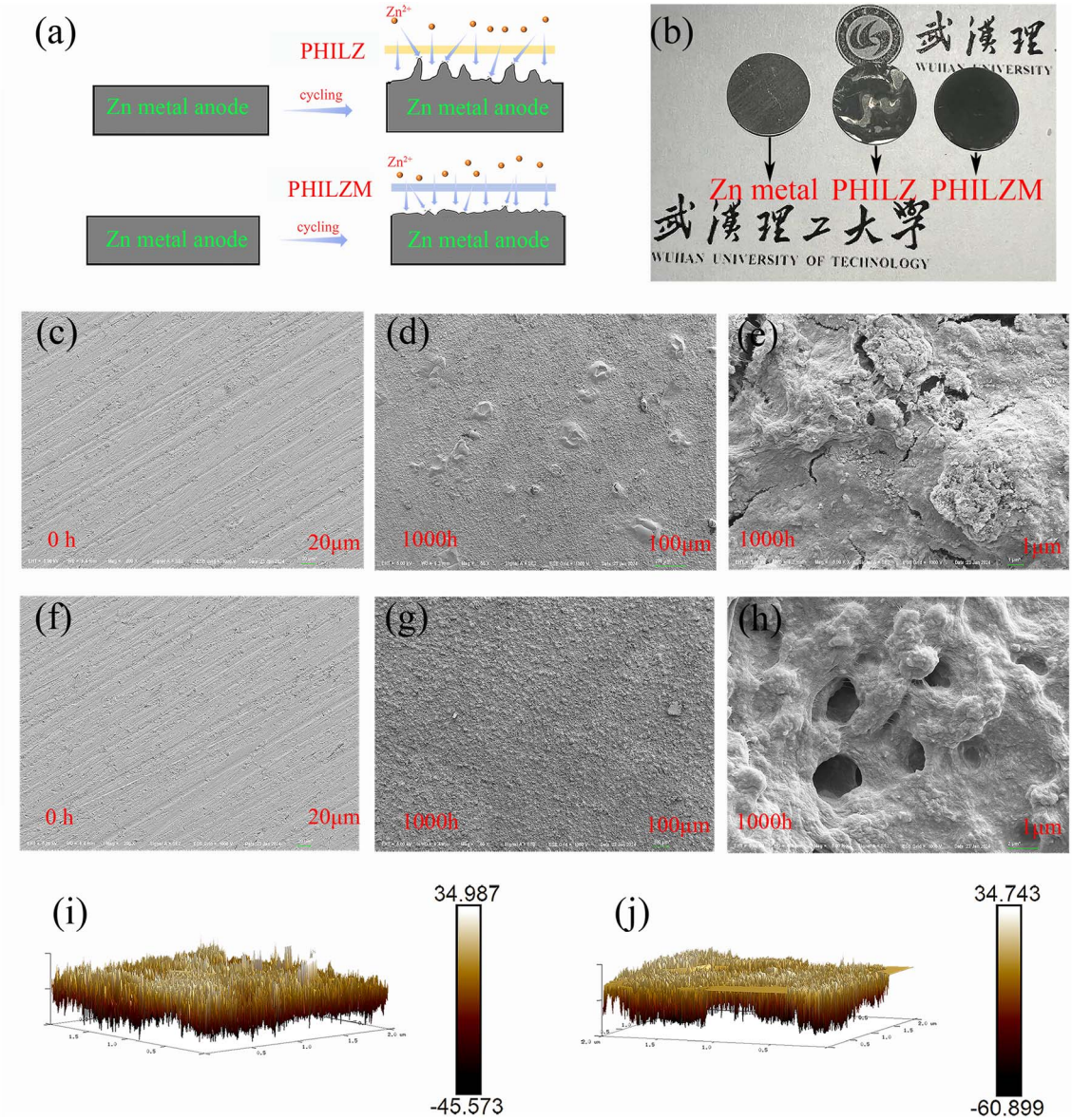

Fig. 5 (a) Schematic of galvanization on the Zn anode. (b) Photograph of zinc anode after 1000 h cycling (from left to right, initial zinc metal, zinc metal after cycling with PHILZ, and zinc metal after cycling with PHILZM). (c) and (f) SEM images of the initial Zn metal surface in the Zn/Zn symmetric cells. (d), (e), (g) and (h) SEM images of the Zn metal surface in the Zn/Zn symmetric cells after cycling 1000 h with PHILZ (d and e), PHILZM (g and h). AFM images of the Zn metal surface in the Zn/Zn symmetric cells after cycling 1000 h with (i) PHILZ, (j) PHILZM.

indicated that PHILZM had a role in regulating ion transport and optimizing ion deposition. As mentioned earlier, ZIF-8 has a highly ordered pore structure and could form a more stable interface with the electrode material, which helped to increase the transmission rate of zinc ions in the electrolyte, reduced the interfacial resistance, and promoted the uniform deposition of Zn^{2+}. This was further confirmed by atomic force microscopy (AFM), where PHILZ (Fig. 5(i)) showed more pronounced spikes compared to the smoother PHILZM (Fig. 5(j)).

Electrochemical performance of full cells

To investigate the full-cell performance, we constructed a ZIB based on a $NaV_3O_8 \cdot 1.5H_2O$ (NVO) cathode, a zinc foil anode, and a gel polymer electrolyte (Fig. 6(a)). The XRD and FTIR spectra of NVO are shown in Fig. S12 (ESI);† the results show that the synthesised NVO matches with those reported in the literature.[75] Fig. 6(b) shows that PHILZM has good multiplication performance. The reversible specific capacities of the full cell with PHILZM reached 262.94, 183.46, 160.45, 141.56, 130.17, and 101.89 mA h g^{-1} at current densities of 0.1, 0.2, 0.4, 0.8, 1.6 and 2.4 A g^{-1}, respectively. At low current densities, button cells assembled with PHILZM were extremely stable and had high specific capacity. When the current density reached 2.4 A g^{-1}, the PHILZ cell almost completely failed, while the capacity of PHILZM remained at 101.89 mA h g^{-1}. When the current was restored to 0.2 A g^{-1}, the capacity reached

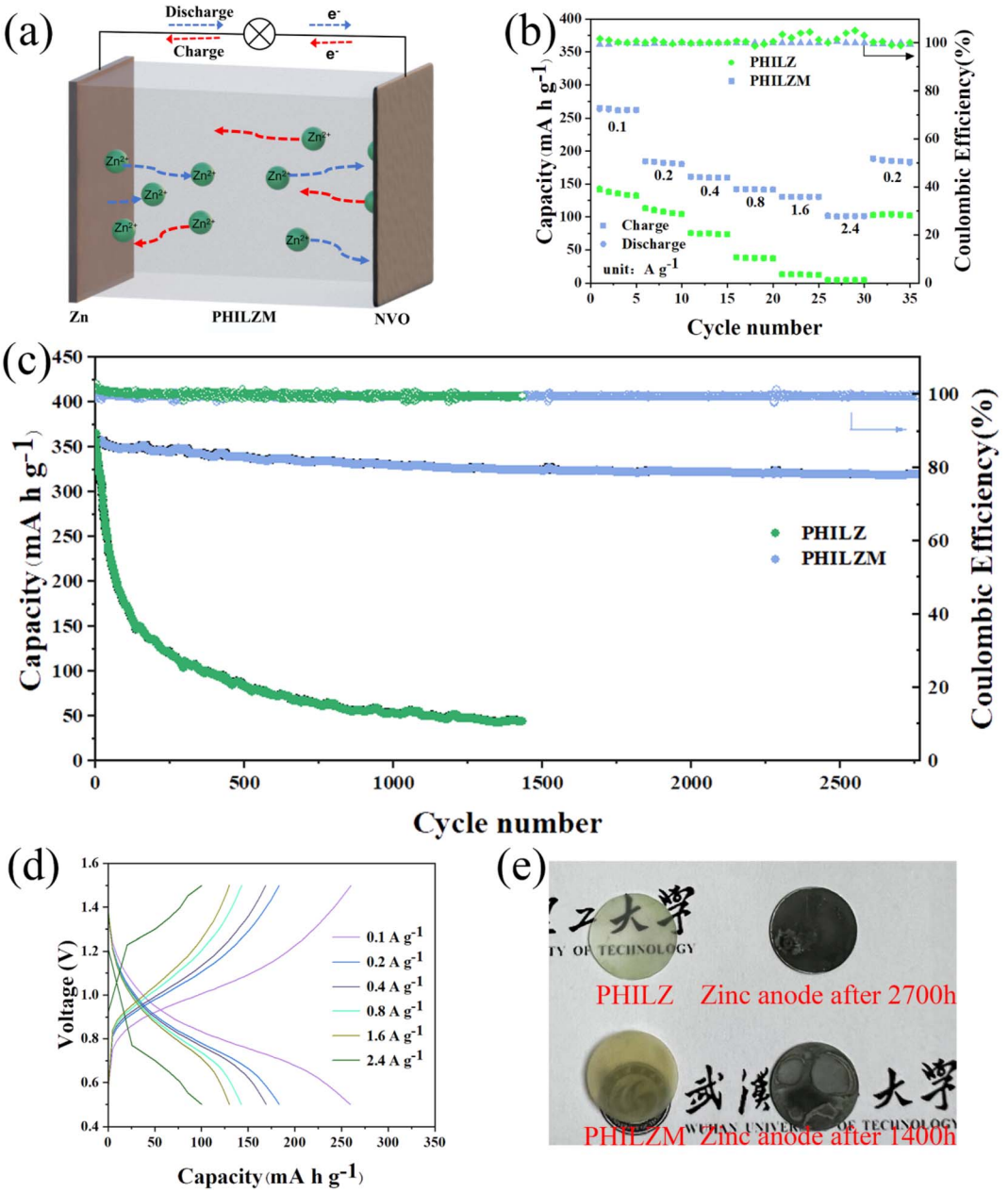

Fig. 6 (a) Schematic of the NVO/PHILZM/Zn full cell. (b) Rate performance of PHILZM and PHILZ. (c) Long-term current cycling performance of the NVO/PHILZM/Zn full cell at 0.05 A g^{-1}. (d) GCD curves of the NVO/PHILZM/Zn full cell at different current densities. (e) Photograph of the electrolyte and zinc anode at the end of the NVO/PHILZM/Zn full cell cycle.

186.99 mA h g^{-1}, and PHILZM had good reversibility. The long cycling ability of the PHILZM full cell was tested to further investigate the cycling stability. As presented in Fig. 6(c), the capacity of NVO/PHILZM/Zn cell was over 350 mA h g^{-1} at 0.05 A g^{-1}, and the average coulombic efficiency was about 99.4%, with a capacity retention of approximately 89.4% even after over 2700 cycles. In contrast, NVO/PHILZ/Zn batteries only lasted about 1400 cycles and had a faster capacity decay.

Fig. 6(d) shows the GCD curves of the button cell assembled with PHILZM at different current densities. A large specific capacity of 260 mA h g^{-1} was achieved at a current density of 0.1 A g^{-1}, and a specific capacity of 100 mA h g^{-1} was obtained even at a high current density of 2.4 A g^{-1}. Fig. 6(e) shows the surface morphology of the zinc metal after cycling of the full cell. The surface of the zinc metal with PHILZM is smoother than the surface of the zinc metal with PHILZ, indicating that the interfacial side reactions between the gel electrolyte and the zinc negative electrode were suppressed. Thus, a good transmission path could be maintained inside the cell to ensure stable charge/discharge cycling. In short, the gel polymer electrolyte had good full-cell long-cycle performance, which was also consistent with the results for the Zn/Zn symmetric cell.

Conclusions

In summary, a MOF-based gel polymer electrolyte (PHILZM) for zinc ion batteries was reported. The addition of the MOF not only improved the conductivity of the gel polymer electrolyte but also inhibited the interfacial side reaction between the gel polymer electrolyte and the zinc negative electrode, thus maintaining a good transport path within the battery and ensuring stable charge/discharge cycles. The ionic conductivity of this electrolyte was significantly higher than most PVDF-HFP-based gel polymer electrolytes that were not doped with MOFs. At −40 °C, PHILZM had a conductivity of up to 1.63 mS cm^{-1}. It is expected to solve the problem of sudden drop in ionic conductivity of the zinc ion battery aqueous electrolyte at low temperature. The Zn/Zn symmetric cell achieved no dendritic formation after 3600 hours at 1 mA cm^{-2}, which is three times higher than that of the gel polymer electrolyte without added MOF. Moreover, the NVO/PHILZM/Zn cell achieved a capacity of 350 mA h g^{-1} at 0.05 A g^{-1} with an average coulombic efficiency of about 99.4% at 2700 cycles, and the cycling stability was also greatly improved compared to PHILZ.

Experimental

Materials

The chemicals used in the synthesis were used as purchased without any further purification. Zinc nitrate hexahydrate ($Zn(NO_3)_2 \cdot 6H_2O$, 98%), 2-methyl imidazole (mIm, 99%), 1-ethyl-3-methylimidazolium tetrafluoroborate ($C_6H_{11}BF_4N_2$, 98%), zinc ditetrafluoroborate hydrate ($Zn(BF_4)2 \cdot xH_2O$, Zn ≥ 18%), vanadium pentoxide (V_2O_5, 99.5%) and poly(vinylidene difluoride-*co*-hexafluoropropylene, PVDF-HFP, m_w = 400 000) were obtained from Aladdin (Shanghai, China).

Synthesis of MOFs

Typically, 2.933 g $Zn(NO_3)_2 \cdot 6H_2O$ (9.87 mmol) was dissolved in 200 mL of methanol. A second solution consisting of 6.489 g of 2-methyl imidazole (79.04 mmol) and 0.1 g diethanolamine (DEA) in 200 mL of MeOH was prepared in parallel. The MOFs were isolated by centrifugation after rapid pouring of the second solution into the former solution with vigorous stirring for 10 min at room temperature. The isolated MOFs were then re-dispersed in methanol and left to stand for several hours before being separated by centrifugation and washed with fresh methanol to give a slightly blue slurry.

Synthesis of PVDF-HFP-based SPEs

Firstly, PVDF-HFP was dissolved in NMP with heating and stirring at 80 °C to obtain a homogeneous solution. Subsequently, the blue slurry was added to the ionic liquid electrolytes (8 mmol zinc ditetrafluoroborate hydrate in 4 mL 1-ethyl-3-methylimidazolium tetrafluoroborate) and stirred until a homogeneous and slightly blue solution was obtained. Finally, the slightly blue solution was added to the PVDF-HFP solution and stirred until homogeneous. For subsequent membrane formation, the fixed-volume slurry was then injected into a Teflon mold. Polymer matrixes were obtained by drying in a vacuum oven at 60 °C to remove the NMP solvent and surplus methanol. These as-prepared matrixes were cut into sheets 16 mm in diameter.

Preparation of the $NaV_3O_8 \cdot 1.5H_2O$ cathode

Commercial V_2O_5 powder (1 g) was added to 15 mL of NaCl aqueous solution (2 M L^{-1}). After stirring for 96 h at 30 °C, the suspension was washed with DI several times. Finally, a black-red product was obtained by freeze-drying.[75] Then, the above sample was mixed with conductive carbon black and PVDF in the organic reagent *N*-methyl-2-pyrrolidone (7 : 2 : 1 weight ratio). After the above mixture was placed on the stainless-steel mesh uniformly and dried at 70 °C for 12 h in the oven, the cathode was acquired through roller pressing the above stainless-steel mesh and punching to disks with a diameter of 16 mm. The loading mass of NVO active material in electrodes was about 2.2 mg cm^{-2}.

Composition and structure characterization

The obtained nanoparticles were characterized *via* dynamic light scattering (DLS, BeNano 90 Zeta), and the morphology was observed using a scanning electron microscope (SEM), JEOL JSM7500 F. N_2 adsorption–desorption isotherms were obtained using a Micromeritics ASAP 2460. Before these measurements, ZIF-8 samples were degassed for 8 h under vacuum at 200 °C using a heating rate of 10 °C min^{-1}. The surface area was calculated using the Brunauer–Emmett–Teller (BET) equation.

Fourier transform-infrared (FT-IR) spectra were recorded using a Nicolet IS10 FT-IR spectrometer resolution in the range of 4000–400 cm^{-1}. The thermal analysis for samples was conducted by using a synchronized thermal analyzer (TG-DSC, HITACHI STA200). For these samples, the temperature was decreased from −80 to 500 °C with a scanning rate of 10 °C min^{-1}. Mechanical properties of solid polymer electrolytes were tested using an electronic universal materials testing machine (Instron 5967).

The initial morphology of the Zn electrode surface and that after cycling were also observed using a scanning electron microscope (SEM,JEOL JSM7500F) and atomic force microscope (AFM, Nanoscope IV).

Electrochemical characterization

The active materials (NVO, $NaV_3O_8 \cdot 1.5H_2O$) were prepared according to literature reports.[75] Electrochemical measurements were carried out in a CR2016 coin cell using zinc foil as the anode and NVO as the cathode.

Cyclic voltammetry (CV) measurements were performed at 1, 5, and 10 mV s^{-1} in the potential window of −0.6–0.6 V with Zn/Ti cells. The ionic conductivities of GPEs were measured using electrochemical impedance spectroscopy (EIS) at temperatures from −70 to 90 °C, in the range of frequency from 10^6 Hz to 10^{-1} Hz and with an alternating current amplitude of 10 Mv using an electrochemical work station with two stainless steel (SS) blocking electrodes. Before each measurement, the sample

was stored for an hour to reach the required temperature. The ionic conductivities (σ) were acquired with eqn (1):

$$\sigma = \frac{L}{R \cdot S}, \quad (1)$$

where R (Ω) is resistance value, L (cm) is the GPE thickness, and S (cm^2) is the cross-sectional area of the SS electrodes. The SS/GPE/SS cell was used to evaluate the electrochemical window of the GPE using linear sweep voltammetry (LSV) at a scan rate of 1 mV s^{-1} and a potential range of 0–3.5 V. The zinc ion transference number ($t_{Zn^{2+}}$) was obtained using a combinational measuring method of AC impedance (10^5 Hz to 10^{-1} Hz) and DC polarization (with a DC voltage of 0.01 V) in symmetrical Zn/GPE/Zn cells and calculated using Bruce–Vincent eqn (2):

$$t_{Zn^{2+}} = \frac{I^S(\Delta V - I^0 R_I^0)}{I^0(\Delta V - I^S R_I^S)}, \quad (2)$$

where ΔV is the applied DC polarization voltage; I^0 and I^S are the initial and stable currents during polarization; R_I^0 and R_I^S are the resistance of the GPE before and after polarization. CV, EIS, DC polarization and LSV were performed on an electrochemical workstation (CHI660E).

The electrochemical data of the batteries were obtained using the CT-4008 Neware Battery Testing System. In the symmetric Zn/Zn battery, long-term cycling properties were tested with two bare Zn foils as electrodes at different current densities (1 and 5 mA cm^{-2}) and surface capacity densities (1 and 5 mA h cm^{-2}). The Zn/NVO full batteries were tested from 0.5 V to 1.5 V with different current densities.

Author contributions

W. C. directed the research. C. H. conceived the project and designed the experiments. C. H. and H. L. carried out the design and fabrication of PHILZM electrolyte. C. H., H. L., Z. T. and Y. L. characterized all the samples. C. H., H. L. and Z. T. performed the electrical measurements. C. W. and C. H. wrote the first manuscript, and all authors discussed and revised the manuscript.

Conflicts of interest

The authors declare no conflict of interest.

Notes and references

1 X. Li, L. Wang, Y. Fu, H. Dang, D. Wang and F. Ran, *Nano Energy*, 2023, **116**, 108858.
2 M. F. Rabbi, J. Popp, D. Máté and S. Kovács, *Energies*, 2022, **15**, 8126.
3 A. Hassan, S. Z. Ilyas, A. Jalil and Z. Ullah, *Environ. Sci. Pollut. Res.*, 2021, **28**, 21204–21211.
4 N. Karimi, L. K. B. Li, M. C. Paul, M. H. Doranehgard and F. Sotoudeh, *RSC Adv.*, 2024, **14**, 9351–9352.
5 H. Wang, Y. Yang and L. Guo, *Adv. Energy Mater.*, 2017, **7**, 1601709.
6 R. Hou, G. S. Gund, K. Qi, P. Nakhanivej, H. Liu, F. Li, B. Y. Xia and H. S. Park, *Energy Storage Mater.*, 2019, **19**, 212–241.
7 Z. Lv, W. Li, L. Yang, X. J. Loh and X. Chen, *ACS Energy Lett.*, 2019, **4**, 606–614.
8 P. Xiao, S. Li, C. Yu, Y. Wang and Y. Xu, *ACS Nano*, 2020, **14**, 10210–10218.
9 J. Shin, J. Lee, Y. Park and J. W. Choi, *Chem. Sci.*, 2020, **11**, 2028–2044.
10 C. Xu, Y. Zhang, N. Zhang, X. Liu, J. Yi, X. Liu, X. Lu, Q. Ru, H. Lu, X. Peng, X. S. Zhao and J. Ma, *Chem.–Asian J.*, 2020, **15**, 3696–3708.
11 T. Mageto, S. D. Bhoyate, K. Mensah-Darkwa, A. Kumar and R. K. Gupta, *J. Energy Storage*, 2023, **70**, 108081.
12 Q. Dai, L. Li, T. K. A. Hoang, T. Tu, B. Hu, Y. Jia, M. Zhang, L. Song and M. L. Trudeau, *J. Energy Storage*, 2022, **55**, 105397.
13 T. Zhang, Y. Tang, S. Guo, X. Cao, A. Pan, G. Fang, J. Zhou and S. Liang, *Energy Environ. Sci.*, 2020, **13**, 4625–4665.
14 J. Yue, S. Chen, J. Yang, S. Li, G. Tan, R. Zhao, C. Wu and Y. Bai, *Adv. Mater.*, 2024, **36**, 2304040.
15 Q. Wen, H. Fu, R. Cui, H.-Z. Chen, R.-H. Ji, L.-B. Tang, C. Yan, J. Mao, K.-H. Dai, X.-H. Zhang and J.-C. Zheng, *J. Energy Chem.*, 2023, **83**, 287–303.
16 Y. Shi, Y. Chen, L. Shi, K. Wang, B. Wang, L. Li, Y. Ma, Y. Li, Z. Sun, W. Ali and S. Ding, *Small*, 2020, **16**, 2000730.
17 Y. Li, C. Zhao, A. Abdukader and X. Wu, *RSC Adv.*, 2024, **14**, 9594–9601.
18 X. Cheng, J. Pan, Y. Zhao, M. Liao and H. Peng, *Adv. Energy Mater.*, 2018, **8**, 1702184.
19 Y. Lv, Y. Xiao, L. Ma, C. Zhi and S. Chen, *Adv. Mater.*, 2022, **34**, 2106409.
20 Z. Ye, Z. Cao, M. O. Lam Chee, P. Dong, P. M. Ajayan, J. Shen and M. Ye, *Energy Storage Mater.*, 2020, **32**, 290–305.
21 P. Xiao, X. Yun, Y. Chen, X. Guo, P. Gao, G. Zhou and C. Zheng, *Chem. Soc. Rev.*, 2023, **52**, 5255–5316.
22 C. Li, X. Yun, Y. Chen, D. Lu, Z. Ma, S. Bai, G. Zhou, P. Xiao and C. Zheng, *Chem. Eng. J.*, 2023, **477**, 146901.
23 H. Liu, Q. Zhou, Q. Xia, Y. Lei, X. Long Huang, M. Tebyetekerwa and X. Song Zhao, *J. Energy Chem.*, 2023, **77**, 642–659.
24 S. Huang, J. Zhu, J. Tian and Z. Niu, *Chem.–Eur. J.*, 2019, **25**, 14480–14494.
25 L. Di, C. Yufang, S. Weiwei, X. Wei, Y. Shuaiyu, L. Shiqiang, Z. Lanlan, Z. Yanshuang, Y. Tianyan, X. Peitao and Z. Chunman, *Adv. Energy Mater.*, 2023, **13**, 2301765.
26 D. Hubble, D. Emory Brown, Y. Zhao, C. Fang, J. Lau, B. D. McCloskey and G. Liu, *Energy Environ. Sci.*, 2022, **15**, 550–578.
27 Y. Xu, W. J. Lin, M. Gliege, R. Gunckel, Z. Zhao, H. Yu and L. L. Dai, *J. Phys. Chem. B*, 2018, **122**, 12077–12086.
28 Q. Li, G. Liu, H. Cheng, Q. Sun, J. Zhang and J. Ming, *Chem.–Eur. J.*, 2021, **27**, 15842–15865.
29 Y. Huang, J. Liu, J. Zhang, S. Jin, Y. Jiang, S. Zhang, Z. Li, C. Zhi, G. Du and H. Zhou, *RSC Adv.*, 2019, **9**, 16313–16319.
30 Z. Li, Y. Chen, X. Yun, P. Gao, C. Zheng and P. Xiao, *Adv. Funct. Mater.*, 2023, **33**, 2300502.

31 J. Hu, Y. Qu, F. Shi, J. Wang, X. He, S. Liao and L. Duan, *Adv. Funct. Mater.*, 2022, **32**, 2209463.
32 Y. Li, J. Yuan, Y. Qiao, H. Xu, Z. Zhang, W. Zhang, G. He and H. Chen, *Dalton Trans.*, 2023, **52**, 11780–11796.
33 R. Qi, W. Tang, Y. Shi, K. Teng, Y. Deng, L. Zhang, J. Zhang and R. Liu, *Adv. Funct. Mater.*, 2023, **33**, 2306052.
34 P. Xiao, Y. Zhao, Z. Piao, B. Li, G. Zhou and H.-M. Cheng, *Energy Environ. Sci.*, 2022, **15**, 2435–2444.
35 X. Tang, S. Lv, K. Jiang, G. Zhou and X. Liu, *J. Power Sources*, 2022, **542**, 231792.
36 K. C. Lethesh, M. O. Bamgbopa and R. A. Susantyoko, *Front. Energy Res.*, 2021, **9**, DOI: 10.3389/fenrg.2021.741772.
37 C. Xu, G. Yang, D. Wu, M. Yao, C. Xing, J. Zhang, H. Zhang, F. Li, Y. Feng, S. Qi, M. Zhuo and J. Ma, *Chem.–Asian J.*, 2021, **16**, 549–562.
38 L. Yu, J. Huang, S. Wang, L. Qi, S. Wang and C. Chen, *Adv. Mater.*, 2023, **35**, 2210789.
39 M. I. Ahmad, D. Bahtiyar, H. W. Khan, M. U. H. Shah, L. Kiran, M. K. Aydinol, M. Yusuf, H. Kamyab and S. Rezania, *J. Energy Storage*, 2023, **72**, 108765.
40 D. Wang, X. Guo, Z. Chen, Y. Zhao, Q. Li and C. Zhi, *ACS Appl. Mater. Interfaces*, 2022, **14**, 27287–27293.
41 Z. Ye, Z. Cao, M. O. Lam Chee, P. Dong, P. M. Ajayan, J. Shen and M. Ye, *Energy Storage Mater.*, 2020, **32**, 290–305.
42 A. Singh, R. Vedarajan and N. Matsumi, *J. Electrochem. Soc.*, 2017, **164**, H5169.
43 X. Yu, N. S. Grundish, J. B. Goodenough and A. Manthiram, *ACS Appl. Mater. Interfaces*, 2021, **13**, 24662–24669.
44 Y. Pan, R. Abazari, B. Tahir, S. Sanati, Y. Zheng, M. Tahir and J. Gao, *Coord. Chem. Rev.*, 2024, **499**, 215538.
45 L. Feng, K.-Y. Wang, J. Willman and H.-C. Zhou, *ACS Cent. Sci.*, 2020, **6**, 359–367.
46 C. P. Raptopoulou, *Materials*, 2021, **14**, 310.
47 M. F. Majid, H. F. Mohd Zaid, C. F. Kait, A. Ahmad and K. Jumbri, *Nanomaterials*, 2022, **12**, 1076.
48 M. Urgoiti-Rodriguez, S. Vaquero-Vílchez, A. Mirandona-Olaeta, R. Fernández de Luis, E. Goikolea, C. M. Costa, S. Lanceros-Mendez, A. Fidalgo-Marijuan and I. Ruiz de Larramendi, *Front. Chem.*, 2022, **10**, 995063.
49 X. Hu, Q. Liu, K. Lin, C. Han and B. Li, *J. Mater. Chem. A*, 2021, **9**, 20837–20856.
50 C.-W. Nan, L. Fan, Y. Lin and Q. Cai, *Phys. Rev. Lett.*, 2003, **91**, 266104.
51 J. Shen, Z. Lei and C. Wang, *Chem. Eng. J.*, 2022, **447**, 137503.
52 C.-Y. Liu, Y.-D. Wang, H. Liu, Q. Chen, X. Jiang, H. Jia and J.-P. Lang, *Composites, Part B*, 2024, **272**, 111227.
53 K. Chaudhary, D. Dhiman, P. Venkatesu and D. T. Masram, *ACS Sustainable Chem. Eng.*, 2022, **10**, 12962–12967.
54 J. Cravillon, R. Nayuk, S. Springer, A. Feldhoff, K. Huber and M. Wiebcke, *Chem. Mater.*, 2011, **23**, 2130–2141.
55 X. Qi, D. Cai, X. Wang, X. Xia, C. Gu and J. Tu, *ACS Appl. Mater. Interfaces*, 2022, **14**, 6859–6868.
56 C. Liu, F. Sun, S. Zhou, Y. Tian and G. Zhu, *CrystEngComm*, 2012, **14**, 8365–8367.
57 R. Dutta and A. Kumar, *Mater. Res. Express*, 2019, **6**, 085305.
58 L. Sangroniz, D. Cavallo and A. J. Müller, *Macromolecules*, 2020, **53**, 4581–4604.
59 X. Gong, J. Wang, Y. Shi, Q. Zhang, W. Liu, S. Wang, J. Tian and G. Wang, *Colloids Surf., A*, 2023, **656**, 130255.
60 L. Zuo, Q. Ma, P. Xiao, Q. Guo, W. Xie, D. Lu, X. Yun, C. Zheng and Y. Chen, *Adv. Mater.*, 2024, **36**, 2311529.
61 L. Tian, Z. Liu, F. Tao, M. Liu and Z. Liu, *Dalton Trans.*, 2021, **50**, 13877–13882.
62 Z. Zhang, M. Liu, C. Li, W. Wenzel and L. Heinke, *Small*, 2022, **18**, 2200602.
63 G. Ortiz, H. Nouali, C. Marichal, G. Chaplais and J. Patarin, *J. Phys. Chem. C*, 2014, **118**, 7321–7328.
64 Y. Xia, N. Xu, L. Du, Y. Cheng, S. Lei, S. Li, X. Liao, W. Shi, L. Xu and L. Mai, *ACS Appl. Mater. Interfaces*, 2020, **12**, 22930–22938.
65 A. K. Nath and A. Kumar, *Solid State Ionics*, 2013, **253**, 8–17.
66 E. Tan, W. Peng, Q. Li, D. Wang, X. Li, J. Duan, H. Guo, G. Yan, J. Wang and Z. Wang, *Electrochim. Acta*, 2024, **473**, 143469.
67 H. Parangusan, D. Ponnamma and M. A. A. Al-Maadeed, *Sci. Rep.*, 2018, **8**, 754.
68 Y. Lei, L. Yue, Y. Qi, Y. Niu, S. Bao, J. Song and M. Xu, *Energy Environ. Mater.*, 2022, **7**, e12511.
69 M. Wang, J. Zhang, X. Yi, X. Zhao, B. Liu and X. Liu, *Appl. Surf. Sci.*, 2020, **507**, 145166.
70 Z. Hao, Q. Zhao, J. Tang, Q. Zhang, J. Liu, Y. Jin and H. Wang, *Mater. Horiz.*, 2021, **8**, 12–32.
71 L. Guo, H. Guo, H. Huang, S. Tao and Y. Cheng, *Front. Chem.*, 2020, **8**, 557, DOI: 10.3389/fchem.2020.00557.
72 M. Wang, A. Emre, S. Tung, A. Gerber, D. Wang, Y. Huang, V. Cecen and N. A. Kotov, *ACS Nano*, 2019, **13**, 1107–1115.
73 X. Liu, J. Liu, B. Lin, F. Chu and Y. Ren, *ACS Appl. Energy Mater.*, 2022, **5**, 1031–1040.
74 L. Cao, D. Li, T. Pollard, T. Deng, B. Zhang, C. Yang, L. Chen, J. Vatamanu, E. Hu, M. J. Hourwitz, L. Ma, M. Ding, Q. Li, S. Hou, K. Gaskell, J. T. Fourkas, X.-Q. Yang, K. Xu, O. Borodin and C. Wang, *Nat. Nanotechnol.*, 2021, **16**, 902–910.
75 F. Wan, L. Zhang, X. Dai, X. Wang, Z. Niu and J. Chen, *Nat. Commun.*, 2018, **9**, 1656.